Fresnel Biprism Common-path Low-coherence Digital Holography for Dynamic Light Scattering Spectroscopy of Biological Materials

GABRIEL GOODWIN,[1,†] DAWITH LIM,[1] SHIVANI MAHAJAN[2] AND DAVID D. NOLTE[1,†,*]

[1]*Dept. of Physics and Astronomy, Purdue University, 525 Northwestern Av., West Lafayette, IN 47907, USA*
[2] *Dept. of Agriculture and Biological Engineering, Purdue University, 225 S University St., West Lafayette, IN 47907, USA*
[†]*These authors contributed equally.*
**nolte@purdue.edu*

Abstract: Doppler frequency shifts associated with the motions in cells range from mHz to Hz, requiring ultra-stable interferometry to capture frequency offsets at several parts in 10^{18}. Common-path interferometers minimize the influence of mechanical disturbances when the signal and reference share common optical elements. In this paper, multi-mode speckle self-referencing via a Fresnel biprism demonstrates frequency stability down to 1 mHz. A low-coherence NIR source creates an OCT-like pseudo-coherence-gate in Fourier-domain holography without phase stepping, and the Fourier reconstruction of the self-referencing speckle fields produces an image-domain autocorrelation of the target. Fluctuation spectroscopy of dynamic speckle is performed on a semi-solid lipid emulsion that captures Brownian thermal signatures and on feline tissue culture that measures active intracellular transport. The extension of biodynamic imaging to lower frequencies opens the opportunity for studies of cell crawling in macroscopic living tissues.

1. Introduction

Common-path interferometry dates to the first interferometer, developed by Francois Arago to measure the refractive index of humid air [1]. The later development of multi-path interferometry by Michelson and others offered improved flexibility in optical design and applications but forfeited mechanical stability. Interferometry in biomedical optics has a wide range of applications, primarily in interferometric biosensors [2], with a major expansion after the development of optical coherence tomography (OCT) in 1991 [3]. Spectral-domain OCT [4, 5] uses an essentially common-path configuration by relying on in-line reflectance and spectral interferometry [6]. Oblique in-line common-path interferometry provides phase information in digital holography [7], and diffraction-based common-path systems work in a similar manner [8-10].

Augustin Fresnel, working with Arago on interferometric systems in the years 1816-1819, devised a simple, high-angle biprism to generate stable interference fringes [1]. The Fresnel biprism has recently been adopted in digital holography to provide a common-path approach to biological imaging in transillumination configurations [11-13]. The monolithic optical element of the Fresnel biprism, combined with wide-field interference, provides higher flexibility for many optical applications. Here, we demonstrate the use of the Fresnel biprism to extend the low-frequency performance of biodynamic imaging, which is a form of digital holographic dynamic-contrast optical coherence tomography [14-17].

Speeds of cellular and intracellular motions span from nanometers per second to microns per second with associated Doppler frequencies in a backscattering optical configuration ranging from mHz to Hz, respectively [18]. At the low-frequency limit of mHz, measurements of metastatic cell crawling within living tissues could have important applications in cancer

research. Current biodynamic imaging configurations have a low-frequency limit of 10 mHz, mainly based on Mach-Zehnder configurations that are susceptible to mechanical motions. These systems become dominated by 1/f noise below 10 mHz. The improved stability of common-path biodynamic imaging systems based on diffraction were used for bacterial infection studies [19], but these systems used a single-mode partial-wave reference, which had low photon efficiency and suffered from slow drifts that limited the stability at low frequencies. The wide-field interference of the Fresnel biprism is an alternative that can extend the system performance to lower frequencies while increasing photon efficiency.

2. Fourier-Plane Digital Holography with a Fresnel Biprism

The Fresnel Biprism is an optical component which consists of a glass element with a planar face and two triangular faces which meet a high apex angle α, forming a small angle $\beta = (\pi - \alpha)/2$ for the exit face. A planar wave propagates through the flat face and refracts across the triangular faces, forming two separate planar waves that propagate in non-parallel directions at angles $\theta \pm (n-1)\beta$. As these plane waves intersect in space, a diamond-shaped region of interference is produced with a spatial frequency given by

$$K = \frac{2\pi}{\Lambda} = \frac{\pi\beta}{\lambda}(n-1) \tag{1}$$

For a circular beam of diameter D incident on the flat face of the Fresnel biprism, the distance at which the interference pattern is of maximum width, denoted by d, is determined using Snell's law, and is given by

$$d = \frac{D}{4}(\cot\theta - \tan\beta) \approx \frac{D}{4\beta(n-1)} \tag{2}$$

and the maximum overlap width, W, is

$$W = \frac{D}{2}(1 - \tan\theta\tan\beta) \approx \frac{D}{2} \tag{3}$$

For interferometric biological imaging using digital holography on the Fourier plane, the fringe spacing and the speckle size on the camera face must satisfy a rule of thumb known as the "rule of nine" that establishes three pixels per fringe and three fringes per speckle to produce a reconstructed cross section of the target approximately in the center of an image-domain quadrant. The design features of the Fresnel biprism in a digital holography system on the Fourier plane are shown in Fig. 1. The "rule of nine" is satisfied by $f\lambda/D = 9p$, where f is the focal length of the Fourier lens, λ is the center wavelength of the light source, D is the diameter of the lens aperture, and p is the pixel size on the camera plane. The maximum overlap distance, d, should be approximately equal to the focal length of the Fourier lens with the maximum width of the overlap approximately equal to the size of the camera sensor, but achieving all these conditions requires design trade-offs.

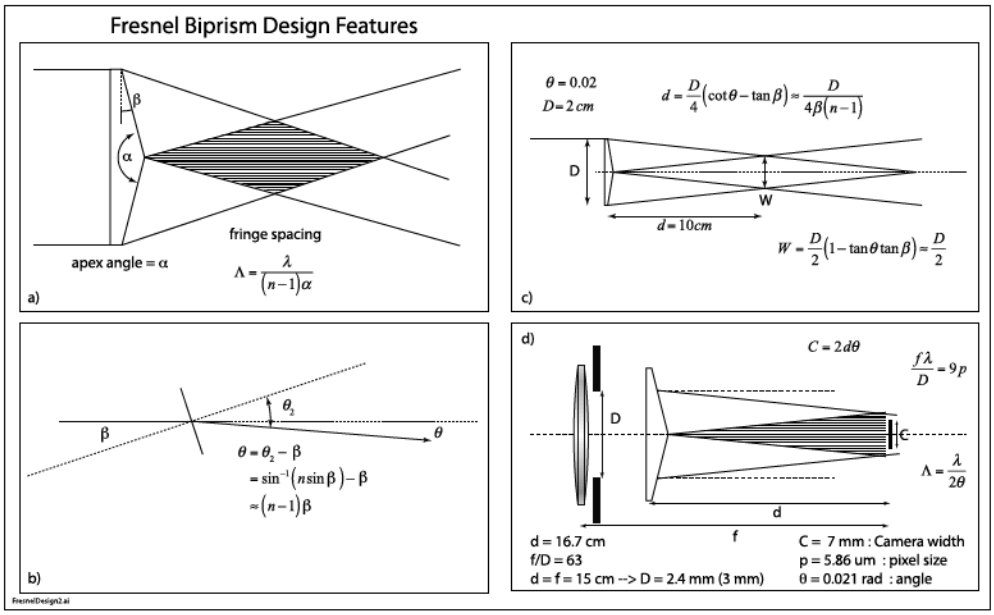

Fig. 1 Design features of the Fresnel biprism combined with digital holography performed with the camera on the Fourier plane.

The camera resides on the Fourier plane, where the two partial fields overlap to form the superposition field

$$E = F^{+}(x+\eta)\exp(iKx/2) + F^{-}(x-\eta)\exp(-iKx/2) \tag{4}$$

where $F^{\pm}(x\pm\eta)$ are the half-plane Fourier fields of the object wave with the spatial shift $\eta = \beta d(n-1)/2 \square D/4$. The hologram intensity is

$$\begin{aligned} H &= \left|F^{+}(x+\eta,y)\exp(iKx/2) + F^{-}(x-\eta,y)\exp(-iKx/2)\right|^2 \\ &= \left|F^{+}(x+\eta,y)\right|^2 + \left|F^{-}(x-\eta,y)\right|^2 \\ &\quad + F^{+}(x+\eta,y)F^{-*}(x-\eta,y)\exp(iKx) + F^{+*}(x+\eta,y)F^{-}(x-\eta,y)\exp(iKx) \end{aligned} \tag{5}$$

where the last two terms are the interferogram. With the camera on the Fourier plane, the Fourier reconstruction of the hologram produces a zero-order signal (Fourier Transform of the first two terms) and two side bands. A reconstructed sideband is given as

$$S^{+} = FT^{-1}\left\{F^{+}(x+\eta,y)F^{-*}(x-\eta,y)\right\} = e^{-2ik\eta} \square O(x,y)O^{*}(x-\tau,y-\sigma)d\tau d\sigma \tag{6}$$

where *O(x,y)* is the object field, and S^{+} is a two-dimensional autocorrelation of the image multiplied by a constant phase factor given by the Fourier shift theorem. A numerical example of a speckled target (the letter A) and the hologram are shown in Fig. 2 with a grating vector tilted at 45°. The numerical reconstruction using an FFT is shown in Fig. 3a on a logarithmic color scale. The zero-order is the incoherent autocorrelation of the target, and the two sidebands are the coherent reconstructions that are phase conjugate pairs. A simulated speckle field representative of a small tumor spheroid is reconstructed in Fig. 3b. The simulation operates

on an 800x800 pixel array, beginning with a two-dimensional image-domain complex-amplitude speckle pattern with a point-spread-function typical of experimental conditions for tumor spheroids. The field-of-view is approximately 90 pixels to generate Fourier-domain speckle widths that span approximately nine pixels. The biprism hologram is generated by splitting the Fourier field in half and overlapping the fields with a superposed spatial phase modulation that produces three pixels per fringe and three fringes per speckle diameter in the "rule-of-nine" condition. The rule-of-nine for Fourier-plane digital holography with the tilted grating vector places the reconstruction in the +1 and -2 quadrants, helping to provide maximum separation of the sidebands from the zero-order without aliasing. The autocorrelation of the target image retains significant spatial information. For instance, in the case of the tumor spheroid, the center of the reconstruction is dominated by photons scattered near the optic axis from the tumor, while the outer rim is dominated by photons scattered from the rim. Therefore, the spheroid symmetry of the target allows an investigation of dynamics in the shell relative to dynamics in the core of the spheroid, which has clinical relevance when studying the effects of anticancer drug therapy on living tissue.

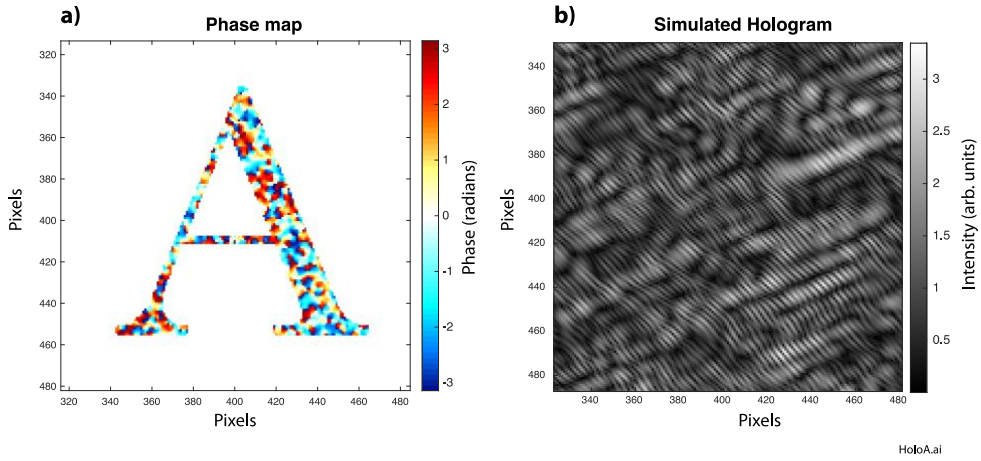

Fig. 2 Simulation of a speckled target letter "A". a) The speckle phase of the target. b) The simulated hologram caused by speckle self-referencing through the Fresnel biprism.

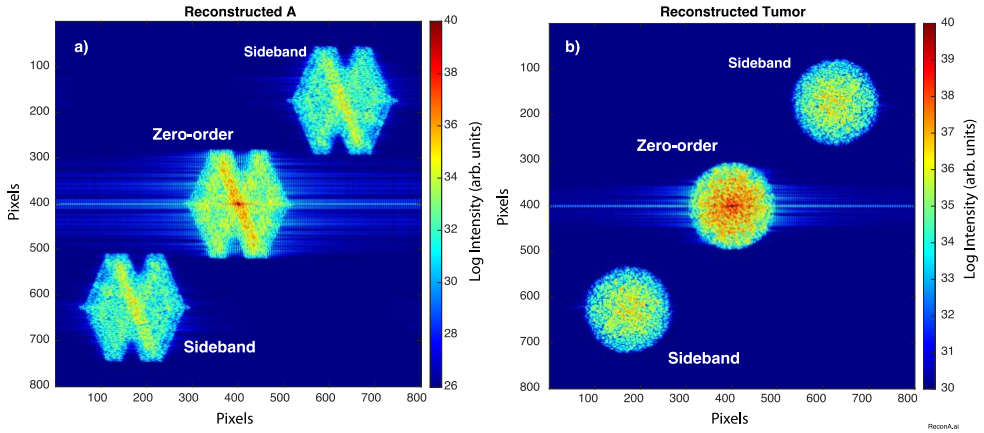

Fig. 3 Simulated reconstructions for a) a speckled letter "A", and b) a tumor spheroid. The two sidebands are phase conjugate pairs, and each is an autocorrelation of the target.

Biodynamic imaging is performed with low-coherence light to provide a coherence gate that selects photons from specified cross sections within volumetric scattering targets such as tumor spheroids. Depth selectivity is achieved by matching optical path length (to within the coherence length of the light source) between the signal photons and a delayed reference wave that is adjusted to a specific depth inside the target. However, the common-path system presented here uses self-interference between the left and right sides of the speckle fields. Interference fringes are generated only between photons that share the same optical path length. Photons that scatter from deeper in the target do not interfere with photons scattered from shallower depths. For a volumetric target such as a tumor spheroid, this produces low-contrast fringes because most of the scattered partial waves are mutually incoherent. Therefore, the fringes that do arise in the hologram are from photon pairs that have matched optical path lengths. Furthermore, if scattering arises predominantly from single hard backscatter, then the matched photons will have scattered from nearly the same depth inside the target.

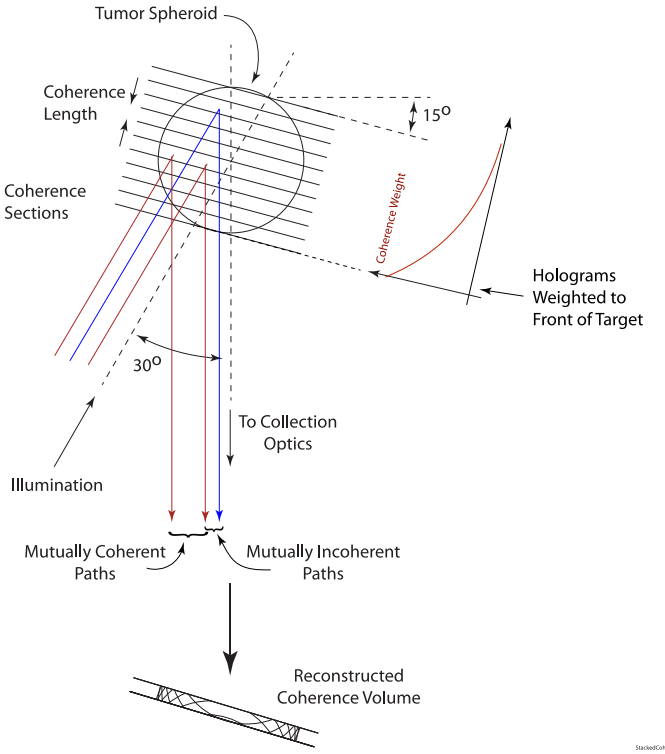

Fig. 4 Illustration of the principle of "stacked" or "compressed" coherence sections in low-coherence speckle self-referencing backscatter holography through a Fresnel biprism. The coherence sections are tilted at half the illumination angle. The reconstructed hologram is an incoherent linear superposition of the coherence sections weighted by the scattered intensity that is strongest for the shallowest layer.

This low-coherence self-referencing causes a form of coherence gating that is "compressed" or "stacked", illustrated in Fig. 4. The reconstructed coherence sidebands are comprised of a superposed stack of optical sections as if the reference in a conventional Mach-

Zehnder BDI system were scanned across the full depth of the target during a single acquisition. The illumination in Fig. 4 is at 30º from the optical axis to prevent specular reflections and to eliminate the need for a beamsplitter. The coherence-gated planes are tilted at half that angle because of optical path length matching at the planar detector. The reconstructed hologram is the linear (and incoherent) superposition of each of the coherence sections. This prevents depth information from be explicitly obtained in this Fresnel biprism system. However, the self-referencing weights the coherence section holograms by the scattered intensity that is strongest from the shallowest sections. This effect weights the reconstructed hologram to approximately three ballistic scattering lengths inside the target, which is approximately 300 microns for a tumor spheroid. This depth is at the boundary between transport-limited tissue that is in under naturally low oxygen tension for an avascular tumor and hyperoxic tissue nearer to the surface of the tumor. This boundary is of particular interest in studies of anticancer drug treatments whose efficacies are affected by oxygen tension.

3. Fresnel Biprism Fourier-Plane Digital Holography

Biodynamic imaging systems are conventionally designed with the reference and sample beams propagating through different spatial paths, interacting with different optical components (such as the Mach-Zehnder interferometer). These designs have proven useful for detecting the Doppler frequency shifts caused by the coherent light scattering of biological processes, but mechanical sensitivity hinders their performance at low frequencies where external vibrations can induce small relative differences in path length, leading to phase shifts and fringe washout. The common-path configuration of the Fresnel Biprism produces fringes from the direct overlapping of two partial speckle fields and should be resistant to external vibrations, creating a more stable system.

The common-path interferometer configuration illustrated in Fig. 5 uses a Fresnel biprism and a Fourier-transform lens that places the digital pixel array on the Fourier plane of the imaging system. The light source is a superluminescent diode (Superlum SLD-381-HP2), which has a center wavelength of 839.6 nm (FWHM of 27.7 nm), delivered at a power of 16.5 mW to the optical system through a single-mode fiber that illuminates the sample from below in an inverted backscattering configuration. The light is captured by an objective lens L1 that transfers the image through a Fourier lens to a digital pixel array on the Fourier plane. The collection optics are mounted at a 30-degree angle relative to the illumination beam to prevent specular reflections from being collected, as discussed in Figure 4. The lens L2, with focal length f2, is mounted a distance f2 away from the image plane of the objective. A camera is mounted at the Fourier plane of this imaging system beyond L2. The camera used in this experiment is a 12-bit FLIR Blackfly S BFS-U3-32S4M camera, which captures 2048 x 1536-pixel images with a pixel pitch of 3.45 microns. The region of interest (ROI) is limited to 800 x 800 pixels for hologram recording. Additionally, the Fresnel Biprism is placed in a mount which orients the interference fringes at an offset angle relative to the pixel array of the FLIR camera.The rule-of-nine discussed in Section 2 dictates, for this pixel pitch, a fringe spacing of 10 microns and a speckle size of 30 microns for optimal results. From this, the geometrical governing equations mentioned in section 2 can be solved for the Frensel biprism apex angle, the focal length of L2, and the beam diameter, which can be controlled with apertures to produce an interference pattern whose maximum width occurs at the Fourier plane where the camera is located, along with being wide enough to be statistically useful. Images on the 800 x 800-pixel footprint require the Fresnel biprism to produce an interfering region with a minimum width of 2.76 mm.

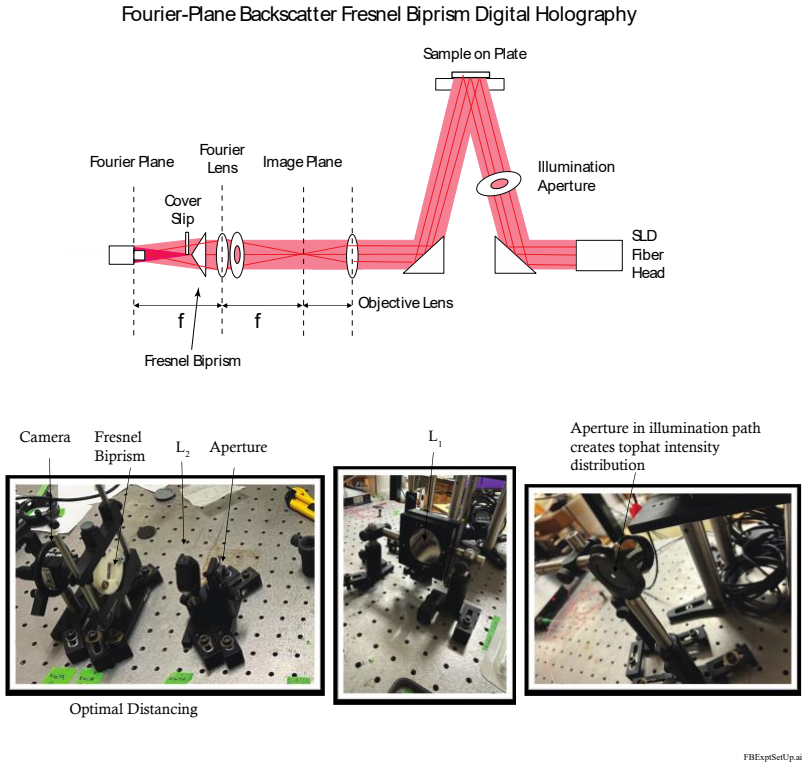

Fig. 5. Fourier-Plane Fresnel biprism digital holography schematic.

Acquiring data from the Blackfly camera is done using the FLIR SpinView Software program. With this software, parameters such as the acquisition frame rate and exposure time are directly controlled. By adjusting nonlinear properties, such as gain, to their default values, the parameter controlling the relative brightness of the acquired images is the exposure time. In this work, a standard of acquiring 3000 frames at a framerate of 3 fps was adopted. The dimmest targets examined which are reported in this work required an exposure time of 300 ms to capture illuminated images. To directly compare different targets with different relative brightnesses, appropriate ND filters were placed in front of L2 to achieve the same relative illumination recorded by the camera when an exposure time of 300 ms was used. The captured images are then analyzed using MATLAB, which converts the 8-bit pixel values saved by the camera to energy values by incorporating the quantum efficiency and saturation capacity of the camera at the light source's 839.6 nm wavelength. Statistics on the saturation and fluctuations of these holograms are calculated, followed by spatial and temporal Fourier transforms, which are used for calculations on the reconstruction of the target (OCI and MCI) as well as the Doppler frequency power spectrum. These yield the signal to noise ratio, fringe contrast, and dynamic range of the sample. The spatial optical coherence image (OCI) and the motility contrast image (MCI) are

$$OCI\left(x,y;t\right)=\left|S^{+}\left(x,y;t\right)\right|^{2}$$
$$MCI\left(x,y\right)=\frac{std_{t}\left(S^{+}\left(x,y;t\right)\right)}{mean_{t}\left(S^{+}\left(x,y;t\right)\right)} \quad (7)$$

where $S^{+}(x,y;t)$ is the side-band reconstruction from Eq.(6) providing the fluctuation speckle image, and the standard deviation and mean are evaluated over time. The MCI is the normalized standard deviation, also known as temporal speckle contrast [20].

For testing purposes, two targets were used as light-scattering standards. Black construction paper served as a static target for which the electronic noise floor of the system can be quantified. A semi-solid lipid emulsion (provolone cheese) served as a Brownian phantom for dynamic light scattering fluctuation spectroscopy. Provolone cheese has low absorbance in the NIR and approximately 80% Lambertian reflectance, providing a stable target with significant multiple light scattering from lipid globules subject to thermal Brownian agitation. An example experimental hologram is shown in Fig. 6 for the paper target. A region of the raw hologram is shown in Fig. 6a) that includes coherent interference fringes as well as incoherent background. The hologram is demodulated by transforming to the Fourier plane where a single sideband is isolated and transformed back to the image plane. The coherent amplitude (absolute value) is shown in Fig. 6b) and the phase in 6c). There are numerous optical vortices as in Fig. 6e), indicated by fringe dislocations that form fork-like patterns, confirming the phase sensitivity in the self-referencing alignment through the Fresnel biprism.

Phase sensitive holography is essential for Doppler fluctuation spectroscopy. The Fourier-plane acquisition of the hologram plays a key role in this phase sensitivity because every resolution element on the image plane is spread over the Fourier lens pupil, ensuring shared spatial coherence between the two halves of the speckle field illuminating the Fresnel biprism. The same system, when operated as image-plane holography with the camera on the image plane, displays perfectly linear fringes with no speckle phase sensitivity. The compatibility between Fourier-plane holography and the Fresnel biprism, with reconstruction using a simple 2D FFT, makes this system ideal for biodynamic imaging applications in biological and biomedical settings.

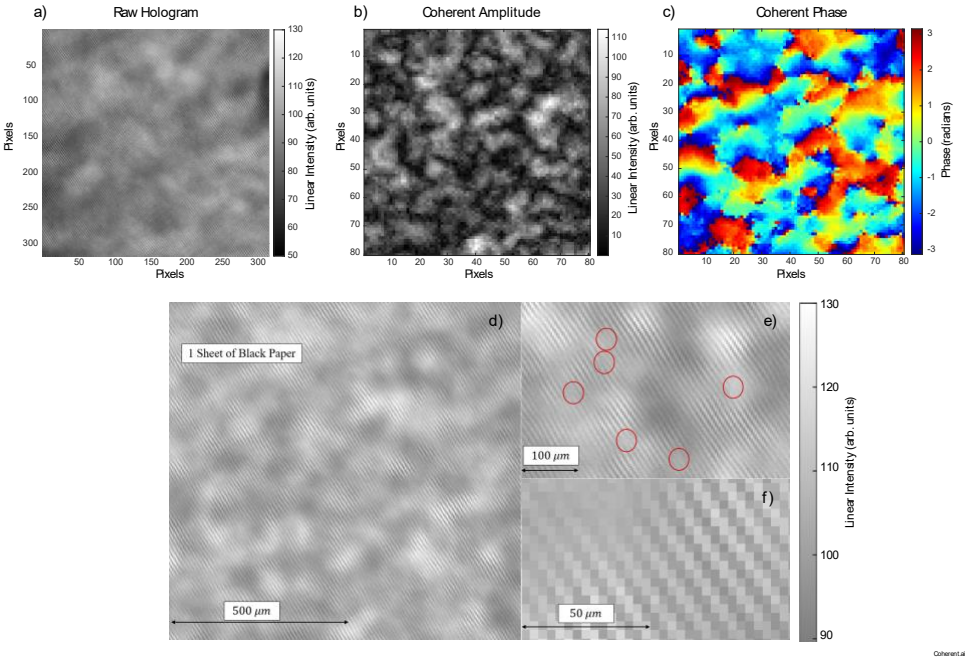

Fig. 6. Hologram of static target (black paper). a) A section of the raw hologram. b) The demodulated amplitude. c) The demodulated phase. d) The raw hologram with a scale label. Optical vortices occur in the fringe patterns in e), demonstrating phase sensitivity. There are approximately three pixels per fringe and at least three fringes per speckle to satisfy the rule-of-nine shown in f).

The raw hologram of the semi-solid emulsion target is shown in Fig. 7a), and the reconstruction using a 2D spatial FFT is shown in Fig. 7b). The tilted fringe spacing produced by the rotation of the Biprism in its mount places the sidebands in opposite quadrants, and the rule-of-nine condition separates the sidebands from the zero-order without aliasing. A line scan through the sidebands and zero-order is plotted in Fig. 7c) on a logarithmic scale. The low-coherence holography displays a fringe contrast of -76 dB (sideband relative to zero-order), and the average signal-to-noise ratio (sideband relative to background) for these tests on static paper is 20 dB. The optical coherence image (OCI) is shown in Fig. 7 d) averaged over 3000 frames at 3 fps with the motility contrast image (MCI) in Fig. 7e). The normalized standard deviation (NSD) for the lipid emulsion is 0.84 caused by multiple dynamic light scattering from the Brownian motion of the lipids. In contrast, the MCI of black paper is shown in Fig. 7f) with an NSD of 0.28 set by the mechanical stability of the holography system.

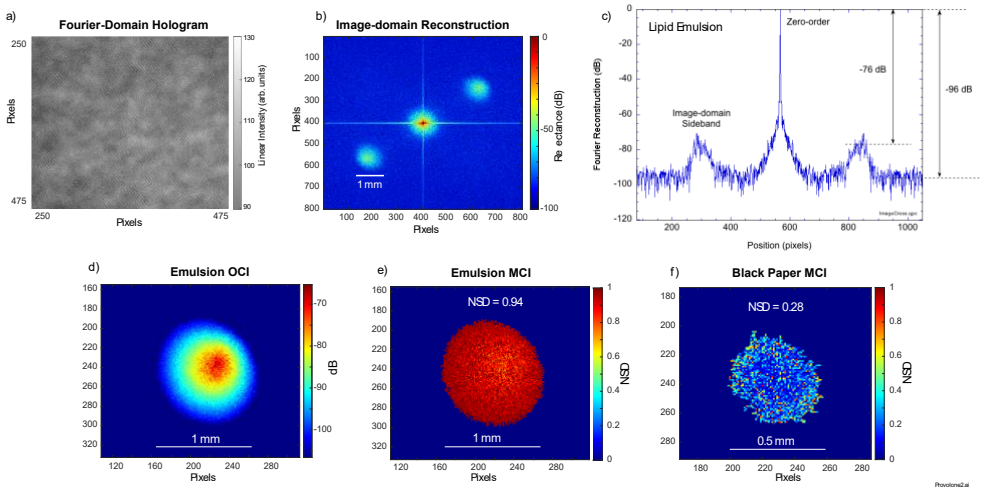

Figure 7. Hologram reconstruction for a semi-solid lipid emulsion. a) Raw hologram zoomed into a 225x255 pixel region. b) The reconstruction plane (image plane) showing the two equivalent sidebands as images. c) A section along the sideband axis plotted logarithmically. d) The optical coherence image (OCI) and e) the motility contrast image (MCI) of the emulsion with NSD = 0.94 compared to f) the MCI for static black paper with NSD = 0.28. Scale bar is 1 mm.

The noise spectra of the phantom targets are shown in Fig. 8 for 3000 frames acquired at 3 fps. The spectral power density is referenced to the DC light intensity averaged over the reconstructed target using a binary mask to exclude contributions from the background. The spectrum of black paper displays classic f^{-n} noise with exponent n varying from 2 to 1 across the spectral range from 1 mHz to 1.5 Hz, establishing the performance noise floor of the system. The lipid emulsion shows two Brownian knee frequencies at 3 mHz and at 30 mHz corresponding to diffusion constants of $D = 6\text{x}10^{-5}$ μm^2/sec and $6\text{x}10^{-4}$ μm^2/sec with viscosity-radius products of $4\text{x}10^{-5}$ Pa•m•sec and $4\text{x}10^{-4}$ Pa•m•sec, respectively. The globule size in cheese ranges from 1 microns to 10 microns, which yields an emulsion viscosity on the scale of approximately 40 Pa•s, which is consistent within an order-of-magnitude of published values [21].

The ability of the Fresnel biprism holography system to be resistant to fringe washout induced by external mechanical vibrations was tested using an iPhone vibration alarm placed on the optical bench in front of the Fresnel biprism. The alarm uses a haptic motor that

generates approximately 2 g's of acceleration with mean displacements of approximately 50 microns at continual 5 Hz vibration. The experimental results shown in Fig. 8 under vibration show no artefacts in the power spectrum, and there were no significant differences in the fringe contrast or signal to noise ratios, although the power spectra revealed slightly increased motion broadly through all frequencies. Under similar conditions, the Mach-Zehnder biodynamic system shows approximately 10 dB fringe washout. Previous BDI systems were limited to 12.2 mHz, below which they were dominated by 1/f noise. The new performance represents a factor of 12x improvement in the frequency floor of the system. It is interesting to note that metastatic cell crawling occurs at speeds below 3 nm/sec with a backscatter Doppler frequency below 10 mHz [18].

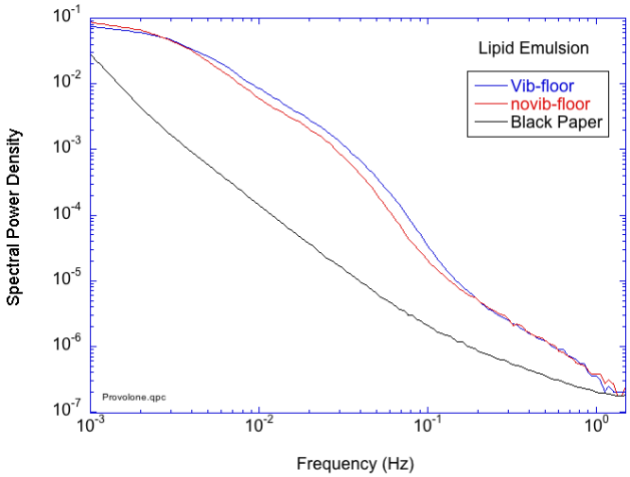

Figure 8. Fluctuation spectrum of semi-solid lipid emulsion compared to static black paper. One spectrum was taken with a haptic motor vibrating on the optical table for conditions that produce fringe washout in a Mach-Zehnder configuration.

4. Biodynamic FB-DH on Living Tissue Spheroids

Biodynamic imaging was originally developed to interrogate living tumor spheroids [22, 23] and living biopsy samples from clinical trials [24, 25]. More recently, studies of microbial infection of tissue culture have yielded to biodynamic imaging [19, 26]. Studies of infection are facilitated by working with smaller tumor spheroids that have higher volume-to-surface ratios. Shifting to small living tumor spheroids approximately 300 microns in diameter is an ideal application for the FB-DH system because the depth-gating is less important in this configuration, and a spatial image is not required for fluctuation spectroscopy which can be performed on an autocorrelation image as produced by the self-referencing.

We prepared several samples of Crandell-Rees Feline Kidney Cells spheroids (CRFK ATCC CCL 94) infected with canine parvovirus (Cornell 780916 80) with $10^{3.77}$ TCID/50 mL. The base medium for the CRFK cell line is composed of 50% RPMI (GIBCO 72400-047), 50% L-15 (GIBCO 31415-029), 10 % fetal calf serum (FCS) and 10 µL of gentamicin. CRFK cells were grown to approximately 2.61×10^3 cells per 25 cm^3 flask. To detach cells from the bottom of the flask they were washed with 3 mL of DPBS (GIBCO 14040133) and then 3mL of TrypLE Express (GIBCO 12604-021). The cells were then put in an incubator set at 37 °C and 5 % CO_2 for 5 minutes to facilitate detachment. The cells along with 50 mL medium were put in two rotary cell culture systems and placed in the incubator for 2 weeks while refilling the medium every couple of days. After two weeks, we added 50 µL of canine parvovirus to one

of the rotary flasks and waited 24 hours. We then took spheroids from each rotary flask (one being control and one infected with virus) at 48, 72, 96 and 120 hours. These spheroids were placed in 16 wells in a 96 well plate with 8 wells being virus infected and 8 wells being control. We added 15 μ*L* of spheroids into each well and then immobilized the spheroids with 80 μ*L* of low melting agarose (0.1 g agarose and 10 mL L-15 medium). We then added 300 μ*L* of complete medium to each well before covering the well with breath-easy sealing membranes.

The image-plane reconstruction of tissue spheroids is shown in Fig. 9. Numerous spheroids fill the approximately 2 mm diameter field of view which is set by the illumination beam profile. The regions of highest intensity are selected with a binary mask, shown in the OCI and the MCI images in Fig. 10a) and b). The OCI color scale is set by the reflectance in dB relative to the average intensity. The MCI color scale is set by the normalized standard deviation (NSD) which measures the temporal speckle contrast with an average NSD of 0.96, and the minimum NSD of approximately 0.8 occurs in the regions of highest spheroid density. These "images" are image-plane spatial autocorrelations of the spheroids within the illuminated field of view.

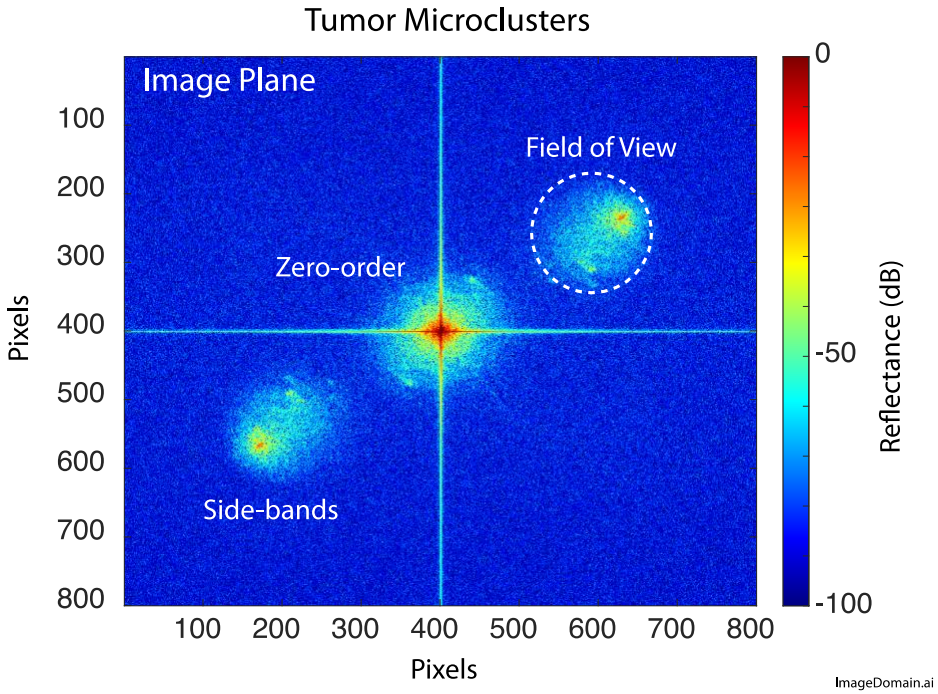

Figure 9. Biodynamic imaging of tumor micro-clusters showing the reconstructed image plane with zero-order and two side-bands that are the optical sections of the target. The reflectance is in dB relative to the maximum pixel value in the zero-order.

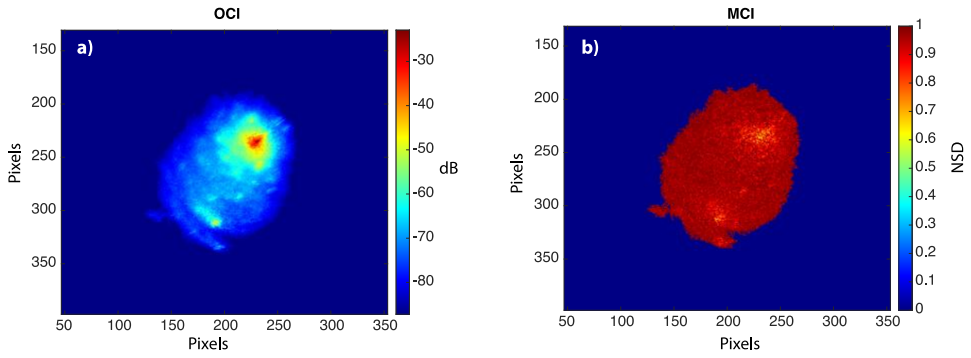

Figure 10. Biodynamic imaging of tumor spheroids. a) The OCI and b) the MCI of the living tissue spheroids after masking.

The performance of the FB-DH system for Doppler spectroscopy is demonstrated in Fig. 11. Three regions on the reconstruction plane were masked off: the tumor region, the zero-order at the center of the reconstruction plane, and a region near the illumination region to characterize the reconstructed background, shown in Fig. 11a). The spectral power density relative to the DC average intensity of three consecutive measurements of spheroid targets are shown in Fig. 11b) for the three regions. The zero-order contains all incoherent intensity fluctuations for non-path-matched optical paths which dominate the acquired intensities on the camera. The tumor region, consisting of the superposed coherence volumes of Fig. 4, shows a pronounced knee frequency near 50 mHz corresponding to an average intracellular speed of 20 nm/sec. The background region shows the noise floor for this measurement, although a small dynamic contribution is remnant from the living tissue that may be from tails on the illumination profile.

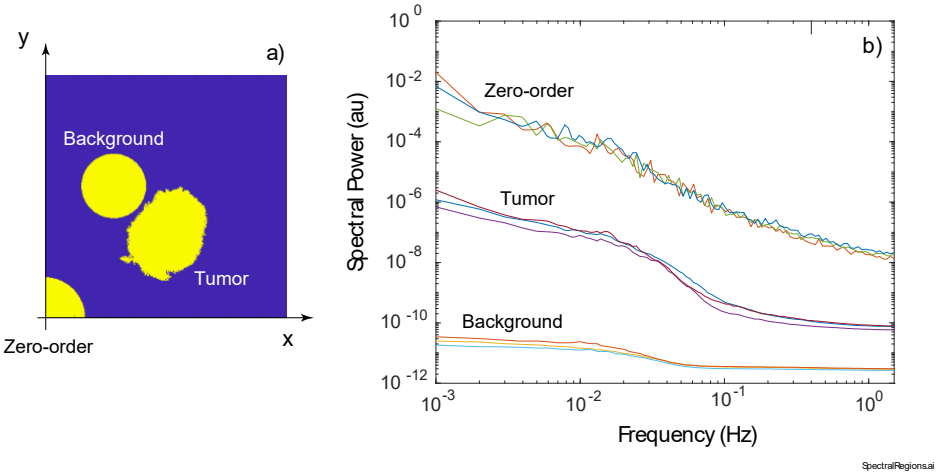

Figure 11. Tissue spectra for feline CRFK tissue spheroids. a) The zero-order, the tumor and the background masks. b) The fluctuation spectra for the masked regions in b).

Of particular interest in microbial infection studies of living tissue is the effect of viral infections on intracellular dynamics. Samples of Parvovirus-infected CRFK were examined

with the Fresnel biprism system. These experiments reveal a significant decrease in activity for Doppler frequencies between approximately 8 mHz and 80 mHz between the CRFK cells infected with canine parvovirus relative to healthy CRFK cells. The high-frequency Nyquist floor is significantly higher for biological samples compared to the electronic noise floor produced by static paper. This is caused by the "strobe" effect in which the fast exposure time captures changes frame-to-frame that appear as the Nyquist floor at the Nyquist frequency.

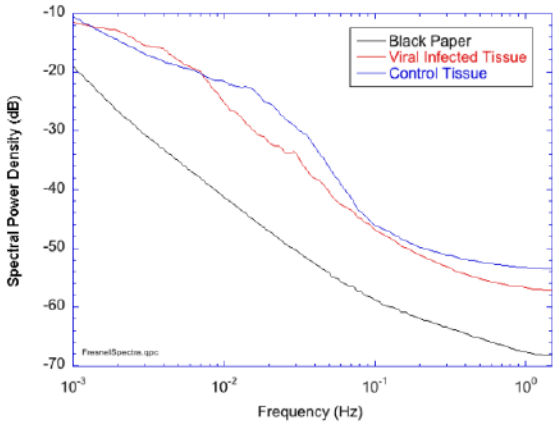

Figure 12. Tissue spectra for feline CRFK tissue spheroids. The spectral power density for healthy tissue spheroids and viral-infected spheroids compared to static black paper.

Maps of the local frequencies across the image plane can be produced by finding the mean frequency for each pixel using the formula

$$\bar{f} = \frac{1}{N} \int_{f_{min}}^{f_{Ny}} f P(f) df \qquad (8)$$

where P(f) is the spectral power spectrum and the integrals are linear in frequency from f_{min} = 1/T to f_{Ny} = fps/2, where T is the total time of the acquisition, fps is the framerate of the acquisition, and N is a normalization constant. The mean frequency is linearly related to the "knee frequency" of the power spectra functions. Pixels with only noise in the power spectrum are vetoed. The resulting frequency map for the CRFK spheroids is shown in Fig. 13a). The frequencies range from 10 to 20 mHz up to approximately 200 mHz. The probability distribution function of the frequencies is shown in Fig. 13b) with many high frequencies (above the average knee frequency for this sample) that are localized to regions of low reflectance. The conditional probability distribution is shown in Fig. 13c) for frequency versus reflectance. There is an inverse relationship between the frequency and the reflectance, where high reflectance is associated with the densest spheroids that are like cohesive tissue rather than a sprinkling of small clusters of cells. We previously verified that the compactness of tissue correlates with spectral knee frequencies, with tighter tissues having suppressed knee frequencies [27]. The lower frequencies for the denser clusters are consistent with this effect.

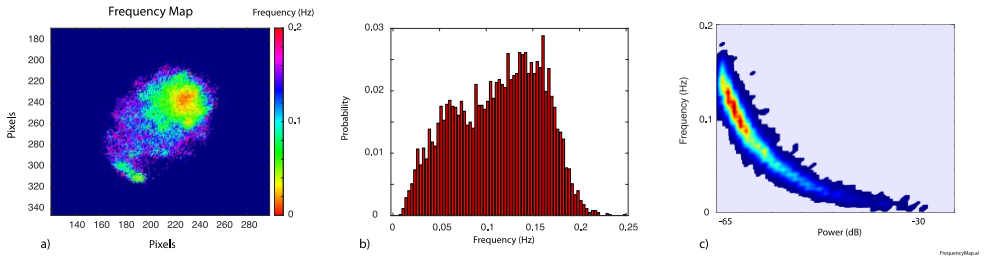

Figure 13. Frequency distributions for CRFK micro-clusters. a) Frequency map. b) Probability distribution function. c) Conditional probability distribution function for frequency as a function of tissue reflectance.

5. Discussion and Prospects

The chief application for biodynamic imaging has been for medium-throughput screening, either of tumor spheroids for drug development or of patient biopsies for cancer chemoresistance screening. In this screening spectroscopy context, neither high-resolution imaging nor depth-gated imaging are necessary. To obtain the highest signal-to-noise, the fluctuation spectra are averaged over the full sample and spatial information is not used. The Fresnel-biprism digital holography (FB-DH) system we report here has the advantage of ultra-stable holographic performance with a new base frequency of 1 mHz that is 12 times lower than in previous biodynamic imaging systems. The trade-offs of losing direct imaging (the image plane reconstruction is a spatial autocorrelation of the target regions) and of losing the OCT-like depth gate (the low-coherence creates a superposed "stack" of coherence volumes) are not central to the spectral averaging used by the biodynamic screening applications. Therefore, for these spectral screening applications, the trade-off is unimportant relative to the improvement in stability and lower frequency performance.

The motivation for retaining the low-coherence light source in the current system is through the pseudo-coherence-gating behavior that is remnant from the low coherence. A long-coherence source (as used in a previous diffraction-based common path system) has the well-known disadvantage of coherent imaging systems, in which light scattered from any components in the optical system can lead to stray interference patterns. For instance, in a recent study using long-coherence in a common-path system, free-swimming bacteria in the liquid medium above tissue micro-clusters contributed to the fluctuation spectra, requiring detailed control experiments to subtract out this effect. With the current low-coherence system, free swimming bacteria in the liquid column above the tissues will not contribute significantly to the fluctuation spectra because of their low reflectance that would preclude the kind of self-referencing coherence gating that does occur from the high reflectance of the tissue sample. Therefore, keeping the low coherence of conventional biodynamic imaging retains some of the depth selectivity that localizes fluctuating signals to tissue depths of 100 to 200 microns.

A particularly exciting future application for the FB-DH system, with its 1 mHz lower frequency limit, is the opportunity to study cell crawling through tissues. Existing 3D tissue-based culture [28, 29] could be augmented with this new velocity-based approach. For instance, immune cells, like T-cells, and metastatic cancer cells crawl through tissue at speeds below 3 nm/sec. The improved stability and low frequency places these processes in a frequency range that now can be measured using dynamic light scattering and fluctuation spectroscopy. For instance, T-cells participate directly in immunotherapy, and the efficacy of different types of immunotherapy drugs could be screened using the FB-DH system. Similarly, anti-metastatic drugs would likely affect metastatic cell crawling, and the new system could provide a means for testing drug efficacy by using light-scattering signatures of the metastatic cell crawling.

In the study of the biological materials presented here, the low-frequency diffusion knees within the lipid emulsion of provolone cheese were observed and related to rheological properties of the material. In the study of feline CRFK cells infected by a canine parvovirus over several days, a pronounced change in the fluctuation spectrum was observable when the viral particles themselves are too small to scatter light. The effect of the virus on the intracellular dynamics are detected through the "sentinel effect" in which the biological agent is measured through its effect on living systems when it cannot be detected directly. These proof-of-concept studies open the door to studies of microbiology and antibiotic resistance.

Funding. Division of Chemical, Bioengineering, Environmental, and Transport Systems (NSF-2200186).

Acknowledgment. The authors gratefully acknowledge the help of Prof. John Turek for advice and help growing the tumor spheroids, and to Fernanda da Cunha and Prof. Michael Ladisch of the LORRE Lab for the cell culture resources.

Disclosure. D. D. Nolte has a financial interest in a company that is seeking to commercialize biodynamic imaging.

Data Availability. Data underlying the results presented in this paper are not publicly available at this time but may be obtained from the authors upon reasonable request.

6. References

1. D. D. Nolte, *Interference: The history of optical interferometry and the scientists who tamed light* (Oxford University, 2023).
2. D. D. Nolte, *Optical Interferometry for Biology and Medicine* (Springer, 2012).
3. D. Huang, E. A. Swanson, C. P. Lin, J. S. Schuman, W. G. Stinson, W. Chang, M. R. Hee, T. Flotte, K. Gregory, C. A. Puliafto, and J. G. Fujimoto, "Optical Coherence Tomography," Science **254**, 1178-1181 (1991).
4. M. Wojtkowski, A. Kowalczyk, P. Targowski, and I. Gorczynska, "Fourier-domain optical coherence tomography: next step in optical imaging," Optica Applicata **32**, 569-580 (2002).
5. S. H. Yun, G. J. Tearney, B. E. Bouma, B. H. Park, and J. F. de Boer, "High-speed spectral-domain optical coherence tomography at 1.3 mu m wavelength," Optics Express **11**, 3598-3604 (2003).
6. L. Lepetit, G. Chriaux, and M. Joffre, "Linear techniques of phase measurements by femtosecond spectral interferometry for applications in spectroscopy," Journal of the Optical Society of America **B12**, 2467 (1995).
7. N. T. Shaked, Y. Z. Zhu, N. Badie, N. Bursac, and A. Wax, "Reflective interferometric chamber for quantitative phase imaging of biological sample dynamics," Journal Of Biomedical Optics **15** (2010).
8. M. Finkeldey, L. Goering, C. Brenner, M. Hofmann, and N. C. Gerhardt, "Depth-filtering in common-path digital holographic microscopy," Optics Express **25**, 19398-19407 (2017).
9. S. H. S. Yaghoubi, S. Ebrahimi, M. Dashtdar, A. Doblas, and B. Javidi, "Common-path, single-shot phase-shifting digital holographic microscopy using a Ronchi ruling," Appl Phys Lett **114** (2019).
10. K. Jeong, M. J. Lopera, J. J. Turek, and D. D. Nolte, "Common-path interferometer for digital holographic Doppler spectroscopy of living biological tissues," Journal of Biomedical Optics **26** (2021).
11. S. Ebrahimi, M. Dashtdar, E. Sanchez-Ortiga, M. Martinez-Corral, and B. Javidi, "Stable and simple quantitative phase-contrast imaging by Fresnel biprism," Appl Phys Lett **112** (2018).
12. S. Ebrahimi, M. Dashtdar, A. Anand, and B. Javidi, "Common-path lensless digital holographic microscope employing a Fresnel biprism," Optics and Lasers in Engineering **128** (2020).
13. C. Hayes-Rounds, B. Bogue-Jimenez, J. Garcia-Sucerquia, O. Skalli, and A. Doblas, "Advantages of Fresnel biprism-based digital holographic microscopy in quantitative phase imaging," Journal of Biomedical Optics **25** (2020).
14. I. Abd El-Sadek, A. Miyazawa, L. T. W. Shen, S. Makita, P. Mukherjee, A. Lichtenegger, S. Matsusaka, and Y. Yasuno, "Three-dimensional dynamics optical coherence tomography for tumor spheroid evaluation," Biomedical Optics Express **12**, 6844-6863 (2021).
15. R. Morishita, I. Abd El-Sadek, P. Mukherjee, A. Miyazawa, K. Tomita, S. Makita, and Y. Yasuno, "Sparse frame acquisition toward fast volumetric dynamic optical coherence tomography imaging," in *Conference on Optical Coherence Tomography and Coherence Domain Optical Methods in Biomedicine XXVI*(San Francisco, CA, 2022).

16. G. Musial, T. Kohlfaerber, H. Schulz-Hildebrandt, G. Huttmann, and P. Steven, "Dynamic contrast microscopic optical coherence tomography as a novel method for assessing corneal epithelium during exposure to benzalkonium chloride," Investigative Ophthalmology & Visual Science **63** (2022).
17. C. Ren, S. Y. Hao, F. Wang, A. Matt, M. M. Amaral, D. Yang, L. Y. Wang, and C. Zhou, "Dynamic contrast optical coherence tomography (DyC-OCT) for label-free live cell imaging," Communications Biology **7** (2024).
18. D. D. Nolte, "Coherent light scattering from cellular dynamics in living tissues," Reports on Progress in Physics **87** (2024).
19. D. Lim, Z. Hua, H. Choi, F. d. Cunha, J. Turek, M. Ladisch, and D. D. Nolte, "Intracellular Doppler spectroscopy of live tissue sentinels for a fast bacterial infection assay," Sci. Rep (submitted) (2024).
20. S. M. S. Kazmi, L. M. Richards, C. J. Schrandt, M. A. Davis, and A. K. Dunn, "Expanding applications, accuracy, and interpretation of laser speckle contrast imaging of cerebral blood flow," Journal of Cerebral Blood Flow and Metabolism **35**, 1076-1084 (2015).
21. M. R. Leach, B. E. Farkas, and C. R. Daubert, "Rheological characterization of process cheese using tube viscometry," International Journal of Food Properties **6**, 259-267 (2003).
22. P. Yu, M. Mustata, J. J. Turek, P. M. W. French, M. R. Melloch, and D. D. Nolte, "Holographic optical coherence imaging of tumor spheroids," Appl Phys Lett **83**, 575-577 (2003).
23. R. An, D. Merrill, L. Avramova, J. Sturgis, M. Tsiper, J. P. Robinson, J. Turek, and D. D. Nolte, "Phenotypic Profiling of Raf Inhibitors and Mitochondrial Toxicity in 3D Tissue Using Biodynamic Imaging," Journal Of Biomolecular Screening **19**, 526-537 (2014).
24. A. Ajrouch, B. Krempley, A. Karkash, J. Dewitt, M. Al-Hadad, D. Lim, D. Nolte, J. Turek, S. Perkins, and S. Jalal, "Evaluating the feasibility and predictive accuracy of biodynamic imaging to platinum-based chemotherapy response in esophageal adenocarcinoma," Front. Oncol. **14**, 1429343 (2024).
25. A. A. Laviana, E. G. Schiftan, J. W. Mashni, M. C. Large, H. Z. Kaimakliotis, D. D. Nolte, J. J. Turek, R. An, T. A. Morgan, and S. S. Chang, "Biodynamic prediction of neoadjuvant chemotherapy response: Results from a prospective multicenter study of predictive accuracy among muscle-invasive bladder cancer patients," Urologic Oncology: Seminars and Original Investigations (2022).
26. H. Choi, Z. Li, Z. Hua, J. Zuponcic, E. Ximenes, J. J. Turek, M. R. Ladisch, and D. D. Nolte, "Doppler imaging detects bacterial infection of living tissue," Communications Biology **4**, 178 (2021).
27. D. Merrill, R. An, J. Turek, and D. D. Nolte, "Digital holography of intracellular dynamics to probe tissue physiology," Applied Optics **54**, A89-A97 (2015).
28. R. M. Kenney, A. Loeser, N. A. Whitman, and M. R. Lockett, "Paper-based Transwell assays: an inexpensive alternative to study cellular invasion," Analyst **144**, 206-211 (2019).
29. J. C. McIntosh, L. Yang, T. Wang, H. B. Zhou, M. R. Lockett, and A. L. Oldenburg, "Tracking the invasion of breast cancer cells in paper-based 3D cultures by OCT motility analysis," Biomedical Optics Express **11**, 3181-3194 (2020).